Epitaxial growth and cationic exchange properties of layered KNb_3O_8 thin films†

A. Waroquet,[a] V. Demange,*[a] N. Hakmeh,[a] J. Perrière,[b] S. Freslon,[a] S. Députier[b] and M. Guilloux-Viry[a]

The KNb_3O_8 potassium triniobate phase is a layered compound that shows excellent photocatalytic activity, intercalation properties and electrochemical performances. In this study, we report the synthesis of this niobate in thin film form. Thin films of layered KNb_3O_8 phase were grown by pulsed laser deposition on (100)-oriented strontium titanate $SrTiO_3$ substrates using targets with different compositions and various deposition parameters. Samples were analyzed by X-ray diffraction, scanning and transmission electron microscopy, X-ray energy dispersive and Rutherford backscattering spectroscopies. This work shows that KNb_3O_8 films are obtained in a narrow composition range, close to $K_{1.13}Nb_3O_{8.7}$ that can be achieved with several combinations of the elaboration parameters (target composition, deposition temperature, target–substrate distance, laser fluence). Slight potassium amount variations in the film composition lead to the growth of other niobates (*i.e.* $K_2Nb_8O_{21}$, $K_6Nb_{10.88}O_{30}$, $K_3Nb_7O_{19}$, $K_4Nb_6O_{17}$). The KNb_3O_8 films are either made of elongated crystals (500 nm long, 50–75 nm wide, and 40 nm thick) or of flat lamellas. In both cases, they are (010)-preferentially oriented with epitaxial relationships with the substrate, namely $(010)KNb_3O_8//(100)SrTiO_3$, $[100]KNb_3O_8//[010]SrTiO_3$ and $[001]KNb_3O_8//[001]SrTiO_3$. Protonation of the KNb_3O_8 films leads to a complete exchange of K^+ ions by H_3O^+ ions that are themselves exchanged by Sn^{2+} ions after immersion in a tin chloride solution confirming the exchange reaction capabilities also in thin films. Exchange of K^+ by Sn^{2+} leads to the band gap reduction of 0.33 eV.

1. Introduction

Layered compounds have received considerable attention for several years due to their numerous catalytic properties, such as intercalation and exfoliation, induced by their particular structure.[1–4] Among these compounds, the KNb_3O_8 potassium triniobate phase (see crystal data in Table 1;[5] energy gap: 3.7 eV)[6] shows luminescence,[7,8] and excellent UV photocatalytic activity for degradation of dyes,[9,10] for catalytic synthesis of monoethylene glycol (used as intermediate for polyester fiber production),[11] and for catalytic reduction of CO_2 in methane.[6] The KNb_3O_8 structure consists of negatively charged $Nb_3O_8^-$ slabs of corner-sharing NbO_6 octahedra with intercalated K^+ ions between the slabs that compensate for the negative charges. In reason of the weak link between K^+ and the $Nb_3O_8^-$

layers, KNb_3O_8 can easily be protonated into $H_3ONb_3O_8$ (sometimes called by mistake HNb_3O_8) by exchange of K^+ by H_3O^+ in acid solution. Further heating of $H_3ONb_3O_8$, that releases one water molecule, leads to the formation of HNb_3O_8.[12] The $H_3ONb_3O_8$ compound also presents interesting photocatalytic properties.[6] In addition, $H_3ONb_3O_8$ can be subsequently exfoliated into $Nb_3O_8^-$ nanosheets that exhibit higher UV photocatalytic activity that their bulk counterpart for degradation of organic contaminants, reduction of CO_2 and decontamination of water.[6,13–20] The $H_3ONb_3O_8$ phase had the ability to exchange the hydronium ion with a high number of cations, including metallic ions and large organic ions.[12,21–27] Some species (2nd guest) cannot be exchanged directly but can be inserted *via* intermediates (1st guest) through a 1st guest–2nd guest exchange reaction.[25,28,29] The cation exchange allows to reach new properties consecutive to the reaction between the host matrix $Nb_3O_8^-$ and the guest ion, like photocatalysis in the visible range,[30,31] the formation of a p–n heterojunction with high performance under visible light for $H_3ONb_3O_8$–$CuNb_3O_8$,[32] and electrochemical performances[25] that are attractive as anode active materials for sodium-ion battery.[33] Several routes have been used to synthesize KNb_3O_8 as single crystal by Czochralski and Bridgman-type methods,[34] and as powder by solid state chemistry,[5,35] molten salts synthesis,[35,36] hydrothermal synthesis,[37] solvothermal synthesis,[8,38] and electrochemical

[a]Institut des Sciences Chimiques de Rennes, UMR 6226 CNRS, Université de Rennes 1/INSA/ENSCR, 263, Avenue du Général Leclerc, 35042 Rennes Cedex, France. E-mail: valerie.demange@univ-rennes1.fr

[b]Institut des Nanosciences de Paris, Université de Paris 1, 4 place Jussieu, 75005 Paris, France

† Electronic supplementary information (ESI) available: RBS spectrum of KNb_3O_8 film on sapphire; XRD, SEM (film D); cross-sectional SEM (films B and D); phi-scan (film E); rocking-curves (films B and E); IR spectra (film F2); EDXS spectra (films F, F2, F3); brightfield micrograph and electron diffraction pattern (film F2); XRD of KNb_3O_8 film on SiO_2; HRTEM (films F, F2). See DOI: 10.1039/c7ra00261k

Table 1 Structural features of the potassium niobates synthesized in this study

Phase	JCPDS card	Space group	Lattice parameters	Ref.
KNb_3O_8	No. 01-075-2182	$Amam$ (no. 63)	$a = 8.903$ Å $b = 21.160$ Å $c = 3.799$ Å	5
$H_3ONb_3O_8$	No. 00-044-0672	Pnn (no. 58)	$a = 9.183$ Å $b = 22.47$ Å $c = 3.775$ Å	12
$K_4Nb_6O_{17}$	No. 01-076-0977	$P2_1nb$ (no. 33)	$a = 7.83$ Å $b = 33.21$ Å $c = 6.46$ Å	48
$K_3Nb_7O_{19}$	No. 01-084-0812	$P\bar{1}$ (no. 2)	$a = 14.1430$ Å $b = 9.948$ Å $c = 6.463$ Å $\alpha = 106.45°$ $\beta = 95.82°$ $\gamma = 97.29°$	49
TTB-$K_6Nb_{10.88}O_{30}$	No. 01-087-1856	$P4/mbm$ (no. 127)	$a = 12.582$ Å $c = 3.992$ Å	50
$K_2Nb_8O_{21}$	No. 00-031-1060	$Pbam$ (no. 55)	$a = 37.461$ Å $b = 12.471$ Å $c = 3.954$ Å	51

synthesis.[39] In polycrystalline materials, it was reported that the KNb_3O_8 particles have an elongated plate-like or wire-like morphology.[10,35,40,41] In reason of this particular morphology, wire-like KNb_3O_8 was used as precursor to obtain by topochemical methods low-dimensional Nb_2O_5 crystals that are of interest for catalysis.[42–44] So far, no synthesis of the KNb_3O_8 phase as film or coating has been reported. By considering the numerous properties of bulk KNb_3O_8, synthesis of such KNb_3O_8 films would be of great interest for applications such as photocatalysis, electrochemistry and intercalation. In this work, we report the synthesis of pure KNb_3O_8 thin films by pulsed laser deposition (PLD), which is commonly used to grow oxide films with complex composition.[45,46] Indeed, in this method a pulsed-laser is used to ablate a ceramic target, and the species emitted by the target during irradiations, condense on the substrate.[45,46] PLD is recognized as a congruent deposition technique, but this method is challenging for potassium-based compound. In fact, due to the high volatility of K_2O, that does not allow a direct stoichiometric transfer from the target to the growing film, at deposition temperature needed for *in situ* crystallization. This high volatility is known to make film features (composition, structure) sensitive to changes of several PLD parameters, as target–substrate distance, temperature or target composition.[45] Therefore, we carefully studied the influence of theses parameters in order to obtain KNb_3O_8 films. Then, we studied and described their epitaxial relationships on (100)$SrTiO_3$. Finally, ion-exchange (H_3O^+, Sn^{2+}) properties were examined for a pure KNb_3O_8 thin film.

2. Experimental section

2.1. Synthesis

Thin films were grown by PLD using a KrF excimer laser (Coherent COMPexPro 102F, pulse duration 20 ns, $\lambda = 248$ nm) operating at 2 Hz with an energy of 210 mJ at two fluence values

(1.85 and 1.95 J cm^{-2}, respectively). The target–substrate distance D_{TS} range was 50–70 mm. During the deposition (30 min), the oxygen pressure (0.3 mbar) was kept constant. Indeed, our previous work on niobates showed that this pressure is favorable to a good quality of crystallization.[45] In the same way, the substrate heater temperature (T) was fixed at 700 °C.

The substrates were 5×5 mm^2 single crystal (100)$SrTiO_3$ ((100)STO), Joint Committee on Powder Diffraction Standards (JCPDS) card no. 01-073-0661; $Pm\bar{3}m$ (no. 221); $a = 3.905$ Å) supplied by Crystal GmbH Company, and were ultrasonically cleaned in acetone during 5 min, then in isopropyl alcohol during 5 min prior to the deposition. Table 2 lists the deposition parameters of 6 of the samples (denoted A to F) synthesized in this study. In order to evaluate the band gap of films before and after cation exchange (see below), a KNb_3O_8 film was grown on a 2 polished faces $10 \times 10 \times 0.5$ mm SiO_2 substrate supplied by Crystec company. The deposition procedure on this substrate was the same than the one used for film F on STO substrate.

As noted in the introduction, the target composition plays an important role in the film composition, and targets with different compositions were used in this work. These PLD targets were prepared by solid state reaction from Nb_2O_5 and K_2CO_3 precursors at 1000 °C in air during 12 h and this synthesis was followed by a sintering of the obtained mixture in air at 1000 °C during 6 h. The precursors were supplied by Alfa Aesar and Acros, respectively. The relative proportions of precursors were prepared with the purpose to obtain targets with various relative cations contents. The target compositions were $K_{0.45}NbO_{2.5}$ (*i.e.* $K_{1.35}Nb_3O_{7.5}$) and $K_{0.5}NbO_{2.5}$ (*i.e.* $K_{1.5}Nb_3O_{7.5}$). Therefore, the ratio between cations amounts (K/Nb ratio) in the targets is equal to 0.45 or 0.5. The real target compositions were measured by energy dispersive X-ray spectroscopy and were found to correspond to what was expected, *i.e.* $K_{0.45}NbO_x$ and $K_{0.5}NbO_x$. Prior to the deposition, the targets

Table 2 Elaboration parameters and characterization results of several KNb_3O_8 thin films on STO with or without other phases (compositions were determined by SEM-EDXS)

Sample	Temperature T (°C)	Target–substrate distance D_{TS} (mm)	Fluence (J cm^{-2})	Target composition	Film composition	K/Nb ratio in the film	Phases
A	700	50	1.85	$K_{0.5}NbO_{2.5}$ ($K_{1.5}Nb_3O_{7.5}$)	$K_{1.18\pm0.12}Nb_3O_x$	0.39	$KNb_3O_8 + K_4Nb_6O_{17} + K_6Nb_{10.88}O_{30}$
B	700	55	1.85	$K_{0.5}NbO_{2.5}$ ($K_{1.5}Nb_3O_{7.5}$)	$K_{1.11\pm0.11}Nb_3O_x$	0.37	$KNb_3O_8 + K_6Nb_{10.88}O_{30}$
C	700	65	1.85	$K_{0.5}NbO_{2.5}$ ($K_{1.5}Nb_3O_{7.5}$)	$K_{1\pm0.1}Nb_3O_x$	0.33	$KNb_3O_8 + K_2Nb_8O_{21}$
D	700	70	1.85	$K_{0.45}NbO_{2.5}$ ($K_{1.35}Nb_3O_{7.5}$)	$K_{0.9\pm0.1}Nb_3O_x$	0.30	$KNb_3O_8 + K_2Nb_8O_{21}$
E	700	70	1.95	$K_{0.45}NbO_{2.5}$ ($K_{1.35}Nb_3O_{7.5}$)	$K_{0.9\pm0.1}Nb_3O_x$	0.30	$KNb_3O_8 + K_2Nb_8O_{21}$
F	700	65	1.95	$K_{0.5}NbO_{2.5}$ ($K_{1.5}Nb_3O_{7.5}$)	$K_{1\pm0.1}Nb_3O_x$	0.33	KNb_3O_8

were polished on dry 320 and 1200 grit SiC papers and cleaned by pulsed dry nitrogen.

2.2. Characterization methods

Samples were observed by scanning electron microscopy (SEM) with two field emission gun Jeol JSM 6310F and Jeol JSM 7100 TTLS instruments working at 7 kV, and at 2 and 5 kV, respectively. Chemical composition of the samples was determined by energy dispersive X-ray spectroscopy (SEM-EDXS) by using a Jeol JSM 6400 instrument operating at 10 kV equipped with an Oxford Inca EDXS system. The samples were coated with carbon prior to this analysis. X-ray diffraction (XRD) characterization of obtained thin films was carried out using a θ–2θ instrument (Bruker AXS D8 Advanced) working with a monochromatized Cu Kα1 radiation and equipped with a 1D detector (192 channels). Data were collected across a 2θ range of 5–80°, using a step of 0.0144° and acquisition time of 180 ms per step. Thin films epitaxy study was carried out using a four circle texture diffractometer (Bruker AXS D8 Discover) operated with Cu Kα radiation in θ–2θ, ω-scan and φ-scan modes, equipped with a 1D detector (192 channels). Transmission electron microscopy (TEM) experiments were performed by using a LaB$_6$ Jeol 2100 instrument equipped with an Oxford Aztec 80 mm^2 SDD device for EDXS analysis (TEM-EDXS). Samples for TEM were prepared by scratching the thin film from the substrate with a diamond tip and by collecting the so-obtained particles on an amorphous carbon copper grid (Agar). Transmission electron brightfield, darkfield micrographs, and electron diffraction patterns were recorded using a GATAN Orius200D CCD (charge coupled device) camera. Rutherford backscattering spectroscopy (RBS) which is well suited for the determination of the composition and thickness of thin films has been used to study the potassium triniobate layers obtained by PLD. For such analyses, a R-plane sapphire substrate (1-102)Al$_2$O$_3$, (JCPDS card no. 00-010-0173; $R\bar{3}c$ (no. 167); a = 4.758 Å, c = 12.991 Å) was used instead of SrTiO$_3$, to avoid the overlapping of the K and Sr and Ti contributions in the RBS spectra. The elaboration parameters of films on sapphire were: target composition $K_{0.45}NbO_{2.5}$, D_{TS} = 60 mm, duration = 10 min (in order to obtain a film thickness about 100 nm, which is mandatory for RBS experiment), fluence = 1.85 J cm^{-2} and T = 700 °C. The RBS experiments were carried out with a 2 MeV He^{2+} ion beam. Absorbance spectra were registered with a UV-Visible Perkin-Elmer and an infra-red

UATR Frontier Perkin-Elmer spectrometers, using a SiO$_2$ substrate as reference.

2.3. Protonation and exchange properties

Ion-exchange of KNb_3O_8 thin films was attempted by using two different methods. A KNb_3O_8 film was immersed in a 0.08 M HCl/SnCl$_2$ solution for 9 days at room temperature (RT) in order to exchange K$^+$ for Sn^{2+} (HCl acid was used to avoid the re-precipitation of the tin chloride). The film was daily rinsed with distilled water, dried in air, and analyzed by XRD. No change was observed except degradation of the film the last day of the immersion. A second KNb_3O_8 thin film (film F) was immersed in a 6 N HNO$_3$ solution for 24 h at RT to exchange K$^+$ for H$_3$O$^+$, then rinsed with distilled water and dried in air, the result of which is referred as film F2. This film was analyzed by XRD and TEM-EDXS. In a second time, the film was immersed in a 0.08 M HCl/SnCl$_2$ solution for 64 h at RT in order to exchange H$_3$O$^+$ for Sn^{2+}. During this experiment, the film was daily rinsed and dried and analyzed by XRD, and subsequently re-immersed in a fresh HCl/SnCl$_2$ solution (film F3). After 64 h, the ion exchange was checked by TEM-EDXS. The same procedure was used with the film grown on silica.

3. Results and discussion

3.1. Growth, phase analysis and morphology

In addition to the KNb_3O_8 phase, there exist several potassium niobates in the Nb_2O_5–$KNbO_3$ phase diagram:[47] $K_4Nb_6O_{17}$,[48] $K_3Nb_7O_{19}$,[49] tetragonal tungsten bronze (TTB) $K_6Nb_{10.88}O_{30}$ phase,[50] and $K_2Nb_8O_{21}$,[51] (see crystal data in Table 1). In this study, more than 20 samples made of either pure KNb_3O_8 phase or KNb_3O_8 phase with these other potassium niobates were synthesized with different combinations of growth parameters: target–substrate distance D_{TS}, substrate temperature T, target composition, laser fluence. In the following, the characterization results of 6 of these samples (denoted films A to F in Table 2) are summarized. The Fig. 1 shows the Nb_2O_5–$KNbO_3$ line (in black) on which the compounds of the phase diagram were reported according to the value of K on Nb ratio (K/Nb ratio) for each of them. From EDXS results, positions of the films were added in red, while positions of the targets appear in blue. The decrease of the K amount relatively to that of Nb in the film compared to that of the target, is due to the volatility of K$_2$O at the deposition temperature.[45] From the XRD, SEM and SEM-
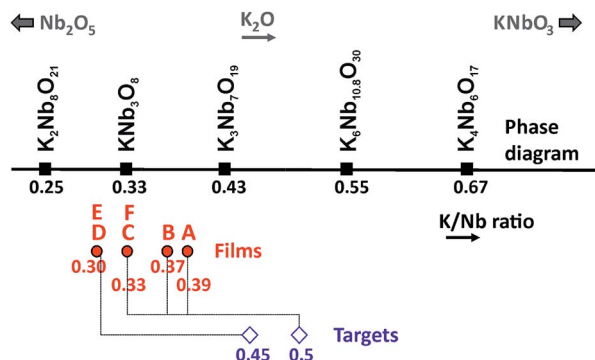
Fig. 1 Scheme displaying the K/Nb ratio in samples A to F, relatively to the K/Nb ratio of the targets used to synthesize these samples, and relatively to the K/Nb ratio of the known niobates of the Nb_2O_5–$KNbO_3$ phase diagram.

EDXS characterization results, it comes that the phase is obtained when the film composition corresponds to a K/Nb ratio ∼ 0.30–0.37, therefore around the stoichiometric composition (K/Nb ratio = 0.33). The RBS analysis (Fig. SI1 ESI†) performed on a pure KNb_3O_8 film gives the $K_{1.13}Nb_3O_{8.7}$ composition (K/Nb ratio = 0.376); this value is close to the stoichiometric formula and close to the result found by EDXS ($K_{1.11\pm0.11}Nb_3O_x$ and $K_{1\pm0.1}Nb_3O_x$ for films B and F, respectively). In all cases, the KNb_3O_8 phase grows on (100)STO with the [010] preferential orientation, i.e. with the $Nb_3O_8^-$ layers parallel to the substrate surface, and no other orientation is observed. The value of the parameter b was measured to be 21.2 Å for all the films, i.e. close to the refined parameter (b = 21.2118 Å) determined by Madaro et al.[35] In addition to the KNb_3O_8 phase, the growth of the $K_4Nb_6O_{17}$ and $K_6Nb_{10.88}O_{30}$ phases is observed (film A, Fig. 2a, Table 2) when the target of composition $K_{0.5}NbO_{2.5}$ is used together with a target–substrate distance D_{TS} = 50 mm.

Thus, the amount of potassium in this film is too high for the targeted compound. It is surprising to observe the growth of the $K_4Nb_6O_{17}$ phase since the composition of the film if far from

that of this compound. Actually, we have observed that this phase has the ability to grow in a very large composition range.[52] To decrease the amount of potassium relatively to that of Nb, a film was synthesized with a higher target–substrate distance (D_{TS} = 55 mm, film B, Fig. 2b). Film B is mainly constituted of the KNb_3O_8 phase. Displaying the intensity of the diagram in logarithmic scale allows to observe a peak located at $2\theta = 22.31°$ (d = 3.98 Å), the intensity of which is 160 counts per s while that of the $(020)KNb_3O_8$ peak is 88 500 counts per s. This peak corresponds to the $(001)K_6Nb_{10.88}O_{30}$ TTB phase, which is therefore still present. From this configuration, additional increase of D_{TS} (Fig. 2c, film C) leads to a depletion of potassium in the film and to the growth of the $K_2Nb_8O_{21}$ niobate.[51,53] Using a target with a lower K amount (films D and E, target $K_{0.45}NbO_{2.5}$, D_{TS} = 70 mm) also leads to the growth of the KNb_3O_8 phase together with a small amount of $K_2Nb_8O_{21}$ (Fig. 2d and SI1†). For these two films, the presence of $K_2Nb_8O_{21}$ is not observed in the XRD diagrams but is evidenced by SEM micrographs (see below). Finally, pure KNb_3O_8 films were obtained from the same target of composition $K_{0.45}NbO_{2.5}$ with a lower target–substrate distance (D_{TS} = 55 mm, film F, Fig. 2e). SEM micrographs display that the microstructure of KNb_3O_8 on STO, for all samples synthesized with a fluence fixed at 1.85 J cm^{-2} (films A–D), is made of elongated and parallelepiped-shaped crystals of dimensions 500 nm in length, and 50–75 nm in width (Fig. 3a–c and SI2 ESI†). Two variants of elongated crystals are observed, corresponding to two in-plane orientations (marked by blue arrows in Fig. 3b), one growing parallel to the [010]STO direction, and the other one at 90° in regards to the first variant.

The samples made at fluence of 1.95 J cm^{-2} (films E and F) have a different morphology. Indeed, they are constituted of macroscopic flat lamellas that are irregular in shape but higher in dimensions (0.5–1 μm) (Fig. 3d). It has been reported that when the fluence is higher, the kinetic energies of ablated species are increased. As a consequence, the fluence is known to affect the growth mode of the film, that follows either the Volmer-Weber mode, with islands formation, (3 dimensions (3D) growth), or Frank–van der Merwe mode (layer-to-layer formation, 2D) or Stranski–Krastanov mode (2D + 3D).[54,55] In the present case, the microstructures displayed in Fig. 3a–c would correspond to the first growth mode, and the morphology of the parallelepiped crystals reflects the anisotropy of the crystal structure. Madaro et al.[35] have synthesized KNb_3O_8 plate-like crystals by molten salt synthesis and shown that morphology of crystals depends both of temperature and salt/oxide weight ratio. They have evidenced that the plates have the [010]-preferential orientation and that the length of the plates grows along the [001] direction. They suggested that this direction which corresponds to the lower connectivity between the corner-sharing NbO_6-octahedra, is perpendicular to the facets with lower surface energy. Indeed, the particle shape is thermodynamically controlled by the Wulff construction which is the surface that minimizes the total surface free energy of a crystal, as a function of crystallographic orientation.[56] Therefore, crystals with anisotropic crystalline structure have generally an anisotropic shape.[57] In the case of flat lamellas (films E
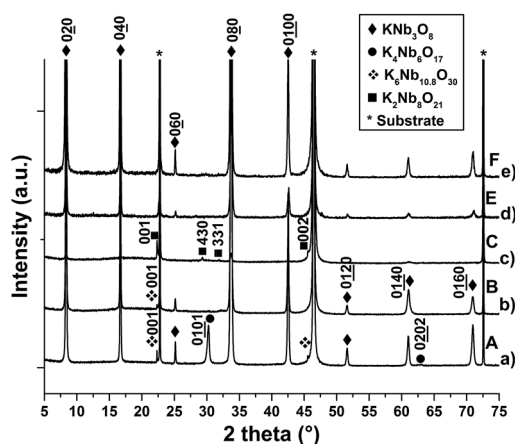

Fig. 2 XRD diagrams in θ/2θ mode of KNb_3O_8 thin films, with or without other phases, grown on (100)STO by PLD with various elaboration parameters (cf. Table 2): (a) film A, (b) film B, (c) film C, (d) film E, (e) film F (substrate: *).
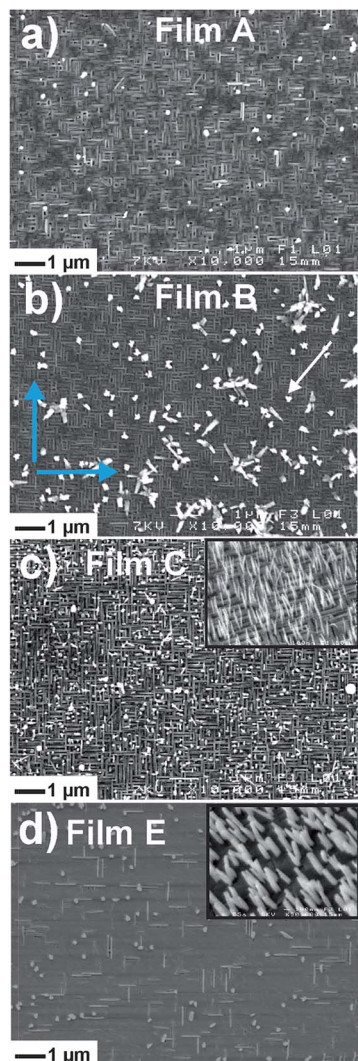
Fig. 3 SEM micrographs of the KNb$_3$O$_8$ thin films, denoted A (a), B (b), C (c), E (d) in text and Table 2, grown on (100)STO. The blue arrows in (b) show the two in-plane elongation directions of the KNb$_3$O$_8$ crystals growing at 90° from each other. The insets in (c) and (d) are SEM micrographs of the films C and E tilted at 45° showing the growth of vertical ribbons and rods.
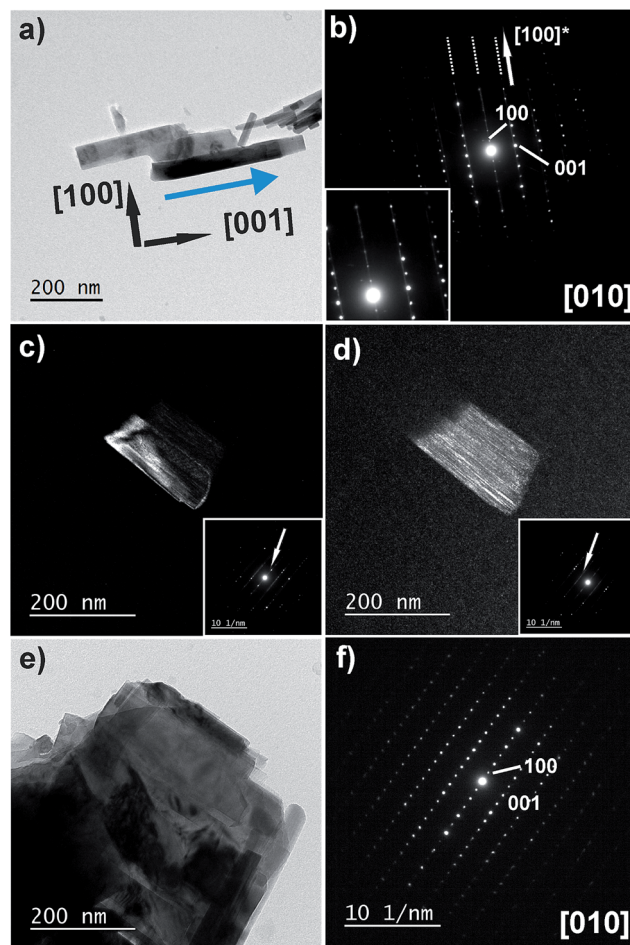

Fig. 4 (a) BF micrograph of some KNb$_3$O$_8$ crystals of the film D; the blue arrow shows the elongation direction of the crystals. (b) Corresponding EDP along the [010] zone axis. Dashed lines show diffusive lines present in the pattern, that can be better seen in the inset. (c) DF micrograph of KNb$_3$O$_8$ crystals obtained by selecting the KNb$_3$O$_8$ (100) reflection labeled by a white arrow in the EDP in the inset. (d) DF micrograph of the same crystals obtained by selecting a diffuse line labeled by a white arrow in the EDP in the inset. (e) BF micrograph of KNb$_3$O$_8$ crystals of the film E. (f) Corresponding EDP along the [010] zone axis.

and F), the growth mode would follow the Frank–van der Merwe mode and the anisotropy of the crystal dimensions is also present, but the films being very flat, the SEM contrast is very low and limits the observation. The thicknesses of the films B and E are about 205–215 nm and 120–135 nm, respectively (Fig. SI3 ESI†).

3.2. Transmission electron microscopy characterization

As shown above, depending on the fluence as a unique parameter, two types of films were observed, differing strongly in their morphology. Also, SEM photographs show some outgrowths perpendicular to the film surface. TEM was used to characterize these features.

   3.2.1. Parallelepiped-shaped films. The Fig. 4a displays a brightfield (BF) micrograph of some KNb$_3$O$_8$ crystals collected

from a KNb$_3$O$_8$ thin film (film D). The corresponding electron diffraction pattern (EDP) (Fig. 4b) shows that the elongation direction of the plate is [001] that confirms the results of Madaro *et al.*[35] and of Kong *et al.*[8] on KNb$_3$O$_8$ particles. Therefore, the shortest lattice parameter *c* is parallel to the longest crystals edge, as also observed for the anisotropic K$_6$Nb$_{10.88}$O$_{30}$ TTB phase.[35,58] The measured lattice parameters by electron diffraction, reported to that of the substrate used as internal standard, are *a* = 8.93 Å and *c* = 3.79 Å, also close to the values refined by Madaro *et al.*[35] in the case of powders. In this EDP, one can observe thin diffusive lines parallel to the KNb$_3$O$_8$ [100]* direction highlighted by white dashed lines in the Fig. 4b and characterized by *d* ∼ 4 Å (see inset in Fig. 4b). In order to more clearly evidence these lines of diffusive scattering, a KNb$_3$O$_8$ crystal was slightly tilted from the [010] zone axis. Darkfield (DF) micrographs (Fig. 4c and d) were then recorded

by selecting the 200 reflection of the KNb_3O_8 phase (inset in Fig. 4c) and a segment of one of the diffusive line (inset in Fig. 4d). These micrographs show that the crystal is actually constituted of stratified layers of well-crystallized KNb_3O_8 slabs that alternate with slabs that are parallel to the $(100)KNb_3O_8$ planes. These slabs are made of another phase that is disordered in the plane parallel to $(100)KNb_3O_8$. Lundberd and Sundberg have also reported very faint streaked pattern of KNb_3O_8 (denoted L-KNb_3O_8 in their work) and have observed that this phase transforms in the solid state to TTB-related phases through an amorphous or poorly crystallized intermediate stage.[59] This phase is possibly the $K_2Nb_8O_{21}$ phase, which is a pseudo-superstructure of the TTB phase.[53] Indeed, d_{001} for $K_2Nb_8O_{21}$ phase is equal to 3.95 Å, and this phase is next to the KNb_3O_8 phase in the phase diagram. The TEM-EDXS analysis performed on several KNb_3O_8 crystals gives the $K_{1.14\pm0.12}Nb_3O_x$ composition (K/Nb ratio ~ 0.38) in agreement with the previous composition analysis.

3.2.2. Flat lamellas films. BF micrograph in the Fig. 4e confirms that the crystals are made of stacking of thin lamellas that are electron transparent, therefore few dozens of nanometers thick. The corresponding EDP (Fig. 4f) shows the [010] zone axis pattern in which no diffuse line is observed, in contrast to film D. Since films D and film E, with same composition, were synthesized with the same deposition parameters except for the fluence, it turns out that this parameter plays also a major role in the crystallinity of the film in addition to its morphology. According to the TEM results of Sundberg and Lundberg,[59] Madaro et al.[35] and Liu et al.,[10] very thin KNb_3O_8 plates are well-crystallized, as for the films E and F made of thin lamellas. Therefore, it could be emphasized that the parallelepipedic shape of KNb_3O_8 crystals in films A to D is related to the intergrowth of poorly crystallized slabs/KNb_3O_8 slabs. Liu et al. have evidenced that photocatalytic performances of KNb_3O_8 compound depend on the crystals shape, and consequently the exposed faces. Indeed, they have shown that very thin flat sheets synthesized by hydrothermal method exhibit higher photocatalytic properties than rod-like crystals synthesized by molten salt method.[10] Therefore, effect of the fluence on the morphology of the thin film crystals is of first importance for their properties.

3.2.3. Identification of outgrowths. On Fig. 3b, one can observe the presence of larger and non-oriented outgrowths on the KNb_3O_8 film, marked by a white arrow. Combination of electron diffraction and darkfield micrographs (TEM experiments) have evidenced that these crystals are nanostructures made of the $K_6Nb_{10.88}O_{30}$ TTB rods (in agreement with our previous results)[58] on which rectangular $K_4Nb_6O_{17}$ plates have grown (not shown).[52] This will be the subject of another article on the growth of the $K_4Nb_6O_{17}$ phase. The TTB rods are (001) preferentially oriented, and correspond to the small (001) XRD peak in Fig. 2b. In Fig. 3c and in inset, one can observe the growth of thin vertical ribbons with their elongation direction parallel to the out-of-plane direction. Similarly, vertical nanorods are observed in Fig. 3d and inset. The dimensions of the nanoribbons are 10–40 nm in width and 400–500 nm in length, while the nanorods are wider (50 nm) and shorter (300 nm).

Electron diffraction experiments (Fig. 5b), performed on 10 different nanoribbons and 10 different nanorods, have evidenced that these nanoribbons and nanorods are actually made of the $K_2Nb_8O_{21}$ phase, with the [001] direction parallel to elongation direction (Fig. 5a), that corresponds to the peak located at $2\theta = 22.42°$ ($d = 3.96$ Å) in the XRD pattern (Fig. 2c). Most of these nanoobjects present structural disorder along (001) planes, as evidenced by diffusion lines in the electron diffraction pattern (Fig. 5b). These results are in agreement with the work of Xu et al. who have synthesized nanoribbons and nanorods of this phase by a molten salt route.[60,61] Recently, Paria Sena et al. have solved the crystalline structure of the $K_2Nb_8O_{21}$ phase in the K–Nb–Ta–O system, and demonstrated that this structure is a pseudo-superstructure of the TTB phase, with the following lattice parameters $a \sim 2\sqrt{2}\ a_{TTB} \sim 37.4$ Å, $b \sim b_{TTB}$, and $c \sim c_{TTB}$.[53] Therefore, both TTB phase and its superstructure have the same growth behavior, i.e. very anisotropic crystal growth with their [001] out-of-plane growth direction corresponding to their elongation direction. Accurate study of the growth of TTB nanorods and of $K_2Nb_8O_{21}$ nanoribbons will be the subject of another article.[52]

3.3. Epitaxy of KNb_3O_8 thin films

Fig. 6a shows the results of the epitaxy study of the (010) oriented KNb_3O_8 phase on (100)STO (film B). Same results were obtained for film E (Fig. SI4 ESI†). The φ-scan performed on the {240} planes of the KNb_3O_8 phase shows 4 peaks separated by 90°, located at the same azimuths that the characteristic peaks of the {110} planes of the STO substrate. As KNb_3O_8 is orthorhombic, these 4 peaks correspond to two in-plane orientation families, the first of it diffracts at 0° and 180°, and the second one at −90° and 90°. This result is consistent with the observation of two types of crystallites elongated along 2 perpendicular directions (Fig. 3a). The coincidence between the lattice of STO and that of KNb_3O_8 is illustrated on the Fig. 6b: the two variants are oriented relatively to the substrate, and the coincidences between the c parameter of each of them with the c and b parameters of STO are schemed by red (variant 1) and blue (variant 2) segments. This epitaxy is governed by the following relationships,
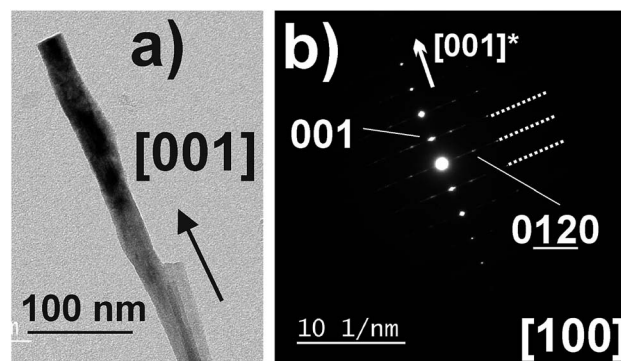

Fig. 5 (a) BF micrograph of a $K_2Nb_8O_{21}$ vertical ribbon. (b) Corresponding EDP along the [100] zone axis. Dashed lines show diffusive lines present in the pattern.

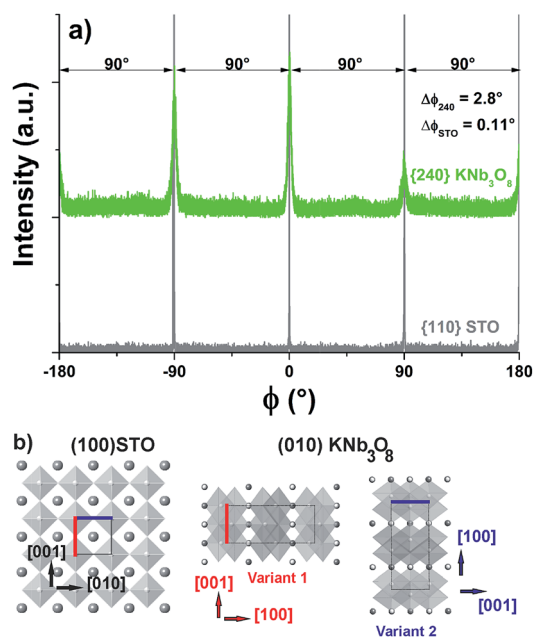**Fig. 6** (a) φ-Scans of the {240} planes of the KNb_3O_8 phase (green line) and of the {110} planes of the (100)STO substrate (grey line) (film B). (b) Scheme of (100)STO substrate and of the two corresponding orientations of KNb_3O_8 crystals on (100)STO (view along the normal to the substrate, *i.e.* along the [010] direction of STO, and along the [010] direction of the KNb_3O_8 phase). The variant 1 is clamped on the substrate in reason of the low mismatch between its c edge relatively to that of the c edge of STO (red segments). The same phenomena is observed for variant 2 (c edge close to b edge of STO, blue segments).

for variant 1:
$(010)KNb_3O_8//(100)STO$
$[001]KNb_3O_8//[001]STO$
$[100]KNb_3O_8//[010]STO$
and for variant 2:
$(010)KNb_3O_8//(100)STO$
$[001]KNb_3O_8//[010]STO$
$[100]KNb_3O_8//[001]STO$

Epitaxial growth is due on one hand to the low mismatch between the lattice parameter of the substrate and the *c* parameter of KNb_3O_8 $((a_{STO} - c_{KNb_3O_8})/a_{STO} \times 100 = 2.7\%)$, and on the other hand, to the low mismatch between 9 lattice units of the substrate and 4 lattice units of the film along the second parameter $((9a_{STO} - 4a_{KNb_3O_8})/(9a_{STO}) = -1.33\%)$. This last relationships belongs to the frame of the domain matching epitaxy, in which *m* lattice units of the film match with *p* lattice units of the substrate. The values of *m* and *p* are defined as the minimum integers which satisfy the relation: $m\,d_{KNb_3O_8} = p\,d_{STO}$, $d_{KNb_3O_8}$ and d_{STO} being the respective atomic distances in the film and substrate parallel directions.[62,63]

The rocking-curve (ω-scan) around the 020 reflection of KNb_3O_8 reveals a medium value of the mosaicity ($\Delta\omega = 1.1°$ for film B, and 1.85° for film E, whereas for STO $\Delta\omega = 0.034°$; Fig.SI5 ESI†) showing some misorientation of this phase on the substrate.

It is probable that the growth of KNb_3O_8 on polycrystalline or amorphous substrates will lead to the [010] preferential

orientation as well, as for other lamellar phases with large interlamellar distance,[64] but with no-ordering in the plane. Therefore, the ability of KNb_3O_8 to grow with an in-plane orientation on a single-crystalline substrate is interesting to increase properties compared to those of textured films.

3.4. Exchange properties

Hosogi *et al.* have shown that the exchanged layered $Sn^{2+}/K_4Nb_6O_{17}$ niobate had visible-range light absorption bands leading to photocatalytic properties under visible light, with a reduction of the energy gap from 3.5 to 2.8 eV.[65] From these results, we studied the ability to exchange K^+ by Sn^{2+} in KNb_3O_8 films. Fig. 7 displays XRD patterns of the film F before protonation (Fig. 7a), after protonation (Fig. 7b and c) and after exchange experiments (Fig. 7d). After a day in nitric acid, the XRD peaks of the film F2 are noticeably shifted to lower angle values and splitted in 3 contributions, labelled by H, H′ and H″ in Fig. 7b. After a few hours in a desiccator, the film was re-examined by XRD, and in the resulting XRD pattern (Fig. 7c), both H′ and H″ peaks have vanished or almost vanished while the intensity of the peaks H was considerably increased. The shift of the 020 peak corresponds to an increase of the intereticular distance d_{020} from 10.59 to 11.23 Å, therefore to an increase of the interlamellar spacing from 21.18 to 22.46 Å. This increase is due to the larger size of the H_3O^+ ion (280 pm, hydrated value) compared to that of the K^+ ion (152 pm). This result is in full agreement with what was observed for a KNb_3O_8 powder after being exchanged in acid nitric to form the $H_3ONb_3O_8$ phase (see Table 1) with an increase of the lattice parameter *b* to the value 22.47 Å.[12,32,42]

The presence of H′ and H″ peaks is most likely due to the intercalation of some species that have induced swelling of the lattice, characterized by an increase of the lattice parameter *b* to 24.68 Å ($d_{020} = 12.34$ Å) and 25.44 Å ($d_{020} = 12.72$ Å), respectively. The vanishing of these H′ and H″ peaks after the stay of the sample in anhydrous atmosphere for a few hours suggests that these intercalated species are probably water and/or
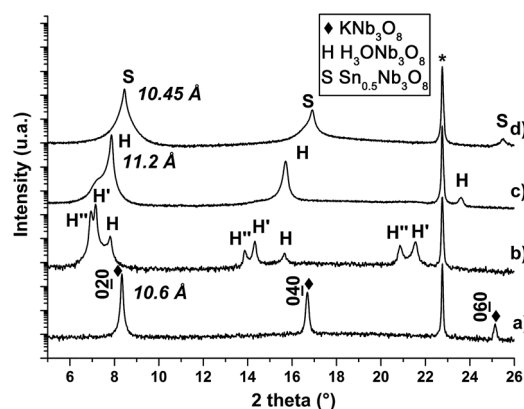

Fig. 7 XRD diagrams in θ/2θ mode: (a) KNb_3O_8 film (film F); (b) same film (F2) after 24 h in a HNO_3 solution (6 N); (c) same film (F3) after 8 h in air in a desiccator; (d) same film after 64 h in a $SnCl_2$/HCl solution (substrate: *).

hydrated hydronium ions, as proposed by Takahashi *et al.* that have observed the same phenomena after the protonation of $KTiNbO_5$ niobate.[66] We performed infra-red spectrometry on a $H_3ONb_3O_8$ film, just after protonation, and after few hours in a desiccator (Fig. SI6 ESI†). Some absorptions bands observed in the spectrum of the just-protonated film are not present for the dehydrated film, as it was reported for other crystalline hydrates, and attributed to water and/or hydrated hydronium ions.[67,68] After dehydration, more matter intercalated with H_3O^+ ions is afterwards diffracting, involving the increase of the peak H intensity in XRD diagram. The film F2 was analysed by TEM-EDXS and found to be fully free of potassium, demonstrating the total exchange of the potassium ions by the hydronium ions (Fig. SI7 ESI†). From TEM, the lattice parameters were measured as being $a = 9.1$ Å and $c = 3.84$ Å (Fig. SI8 ESI†). Fig. 7d shows the XRD pattern of the $H_3ONb_3O_8$ film subsequently immersed 64 h in a tin chloride solution (film F3). The evolution of the XRD patterns of this film was checked daily and was no longer modified after 3 days in the solution. It is observed that the 020 peak shifts now to a higher angle value, corresponding to a decrease of the intereticular distance from 11.23 Å ($b = 22.46$ Å) to 10.45 Å ($b = 20.9$ Å). This results corresponds to the decrease of the radius of the intercalated ion (83 pm for Sn^{2+}) relatively to that of H_3O^+. The Fig. 8a shows the EDP of a part of the film after the two exchange reactions, corresponding to the diffraction of several crystals. By using a smaller selected area aperture, contribution of both variants are separated in Fig. 8b and c. These patterns are close to that displayed in Fig. 4f, with the lattice parameters $a = 9.23$ Å and $c = 3.93$ Å that are slightly higher than the values of the parent phase $H_3ONb_3O_8$, and show that the crystallinity of the phase was preserved. DF micrographs taken by selecting a reflection for each variant (Fig. 8d and e) show that the microstructure built from of rectangular lamellas growing at 90° from each other is also preserved. The Fig. SI7 ESI† shows the TEM-EDXS spectra of film F3 compared to that of the films KNb_3O_8 and $H_3ONb_3O_8$, demonstrating the complete exchange of K^+ by Sn^{2+}. The composition measured by TEM-EDXS is about $Sn_{0.6}Nb_3O_x$, therefore close to what is expected for a complete exchange with respect of electroneutrality. These two exchange reactions were carried out at room temperature, without stirring and in a relative short time, relatively to other exchange reactions performed on powder that take 2–3 days for protonation[6,12,19] and several days for exchange.[12,23]

Fig. SI9 ESI† shows that the thin film grown on silica with the same deposition parameters than the film F grown on STO is a single-phase (010)KNb_3O_8 film. As emphasized above, the film is (010) preferentially oriented even if the substrate is amorphous. This film was successfully protonated before exchange of the potassium ions for the tin ions as shown in Fig. SI9 ESI.† In order to determine if crystal damage results from the exchange, we have performed high resolution transmission electron microscopy (HRTEM) on the KNb_3O_8 film, and on the $SnNb_3O_8$ film (Fig. SI10 ESI†). The micrographs and their fast Fourier transforms show that the $SnNb_3O_8$ film does not present crystal damage. Fig. 9 shows the absorbance spectra of the KNb_3O_8 thin film grown on silica, before and after protonation, and after exchange. The spectra of the $H_3ONb_3O_8$ and $Sn_{0.5}Nb_3O_8$ films are red-shifted relatively to that of the KNb_3O_8 film towards the visible range. The corresponding energy gaps were estimated to be 3.9 eV for KNb_3O_8 film (for 3.7 eV for powder),[6] 3.78 eV for $H_3ONb_3O_8$ film, and 3.57 eV for $Sn_{0.5}Nb_3O_8$ film. The effect of Sn exchange on the oxide band gap value was previously studied for the other layered potassium niobate in this system, *i.e.* $K_4Nb_6O_{17}$ compound, by Hosogi *et al.*[65] These authors reported that the $Sn^{2+}/K_4Nb_6O_{17}$ gap was 0.7 eV narrower than that of $K_4Nb_6O_{17}$, while in the present work, $Sn_{0.5}Nb_3O_8$ film gap was narrower of only 0.33 eV. Nevertheless, these first results are promising for synthesis of
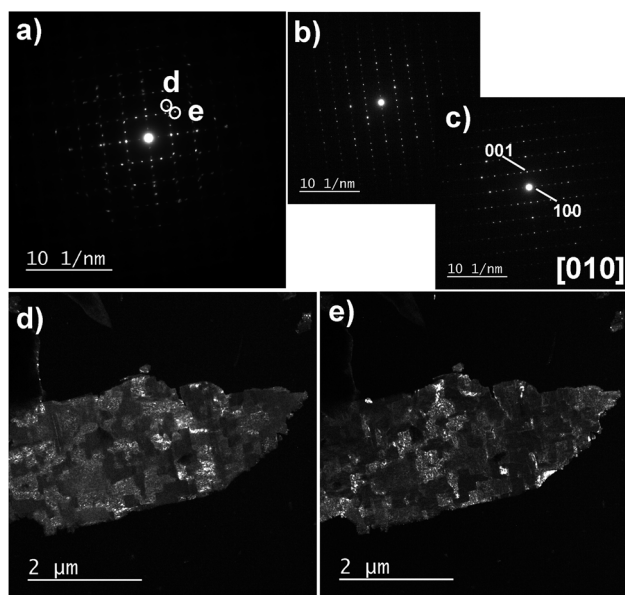

Fig. 8 (a) EDP of a part of the film F3, *i.e.* film F after protonation and intercalation. (b and c) EDPs registered in the same area with a smaller SAED aperture, showing [010] zone axis of two $SnNb_3O_8$ crystals oriented at 90° from each other. (d and e) DF micrographs obtained by selecting the {401} reflections labeled by the letters (d) and (e) in Fig. 8a.
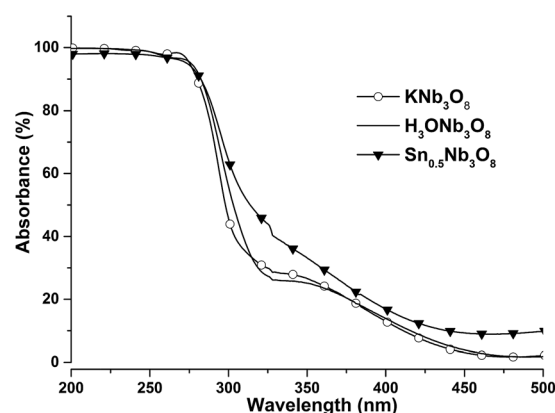

Fig. 9 Absorbance spectra of KNb_3O_8, $H_3ONb_3O_8$ and $Sn_{0.5}Nb_3O_8$ films.

exchange-Nb_3O_8 films with visible-range activity. According to the large amount of species that were intercalated in KNb_3O_8 powder in the past, the present results are also promising for formation of new intercalated KNb_3O_8 thin films for numerous applications as catalysis, electrochemistry, depollution of waste water, *etc.* In addition, lamellar-shaped films are expected to show better photocatalytic properties than the rod-shaped films. Indeed, the effect of the shape of powder KNb_3O_8 and HNb_3O_8 crystals on photocatalytic properties was recently studied by Li *et al.* and Liu *et al.*[6,10] Both groups found that belt shaped crystals present higher photocatalytic properties than the rod-like crystals.

4. Conclusions

Thin films of epitaxially grown KNb_3O_8 phase were synthesized by PLD, with the ability to change the morphology of the crystals constituting the film, from parallelepiped-shaped rods to thin lamellas, by changing the laser fluence. The rods are actually built from alternated slabs of KNb_3O_8 phase and of a poorly crystallized $K_2Nb_8O_{21}$ phase. On the contrary, the lamellas are single phased and well-crystallized and present larger dimensions. We believe that this lamellar morphology of the film would be benefit on the properties as it was observed in the past for KNb_3O_8 crystals synthesized by molten salt method. The ability to exchange K^+ by H_3O^+ and then Sn^{2+} was observed for KNb_3O_8 films, leading to potential properties based on intercalation of various species in the $Nb_3O_8^-$ matrix as it was reported for powder. Perspectives of this work is to study these intercalation properties on cheaper polycrystalline and amorphous substrates, and also by low temperature deposition methods as chemical solution deposition.

Acknowledgements

References

1 G. Centi and S. Perathoner, Workshop Innov. Appl. Layer. Mater. Catal. Nanotechnol., *Microporous Mesoporous Mater.*, 2008, **107**, 3–15.

2 V. Nicolosi, M. Chhowalla, M. G. Kanatzidis, M. S. Strano and J. N. Coleman, *Science*, 2013, **340**, 1226419.

3 M. H. Han, E. Gonzalo, G. Singh and T. Rojo, *Energy Environ. Sci.*, 2015, **8**, 81–102.

4 R. Ma and T. Sasaki, *Acc. Chem. Res.*, 2015, **48**, 136–143.

5 M. Gasperin, *Acta Crystallogr., Sect. B: Struct. Crystallogr. Cryst. Chem.*, 1982, **38**, 2024–2026.

6 X. Li, H. Pan, W. Li and Z. Zhuang, *Appl. Catal., A*, 2012, **413–414**, 103–108.

7 G. Blasse and F. Vantol, *Solid State Commun.*, 1995, **95**, 465–468.

8 X. Kong, D. Hu, P. Wen, T. Ishii, Y. Tanaka and Q. Feng, *Dalton Trans.*, 2013, **42**, 7699–7709.

9 G. Zhang, J. Gong, X. Zou, F. He, H. Zhang, Q. Zhang, Y. Liu, X. Yang and B. Hu, *Chem. Eng. J.*, 2006, **123**, 59–64.

10 X. Liu, W. Que and L. B. Kong, *J. Alloys Compd.*, 2015, **627**, 117–122.

11 Z. J. Yang, Y. F. Li, Q. B. Wu, N. Ren, Y. H. Zhang, Z. P. Liu and Y. Tang, *J. Catal.*, 2011, **280**, 247–254.

12 R. Nedjar, M. Borel and B. Raveau, *Mater. Res. Bull.*, 1985, **20**, 1291–1296.

13 A. S. Dias, S. Lima, D. Carriazo, V. Rives, M. Pillinger and A. A. Valente, *J. Catal.*, 2006, **244**, 230–237.

14 A. Takagaki, C. Tagusagawa, S. Hayashi, M. Hara and K. Domen, *Energy Environ. Sci.*, 2010, **3**, 82–93.

15 S. Masud, M. Zarei, M. L. Lopez, J. Gardea-Torresdey, C. V. Ramana and G. B. Saupe, *Mater. Sci. Eng., B*, 2010, **174**, 66–70.

16 T. Shibata, G. Takanashi, T. Nakamura, K. Fukuda, Y. Ebina and T. Sasaki, *Energy Environ. Sci.*, 2011, **4**, 535–542.

17 M. Zarei-Chaleshtori, M. Hosseini, R. Edalatpour, S. M. S. Masud and R. R. Chianelli, *Microchem. J.*, 2013, **110**, 361–368.

18 P. Zhou, Q. Li, J. He, D. Li and Z. Li, *Russ. J. Phys. Chem. A*, 2015, **89**, 2097–2104.

19 N. Lee and Y.-M. Chung, *Appl. Surf. Sci.*, 2016, **370**, 160–168.

20 S. Liang, L. Wen, S. Lin, J. Bi, P. Feng, X. Fu and L. Wu, *Angew. Chem.*, 2014, **126**, 2995–2999.

21 X. Wang, W. Hou, H. Wang and Q. Yan, *Catal. Commun.*, 2002, **3**, 275–280.

22 N. Belmokhtar, R. Brahimi, R. Nedjar and M. Trari, *Mater. Sci. Semicond. Process.*, 2015, **39**, 433–440.

23 V. R. L. Constantino, M. A. Bizeto and H. F. Brito, *J. Alloys Compd.*, 1998, **278**, 142–148.

24 T. Nakato, K. Kuroda and C. Kato, *Chem. Mater.*, 1992, **4**, 128–132.

25 S. Wang, C. Liu, L. Liu, X. Zhang, J. Gong and Z. Tong, *Synth. React. Inorg., Met.-Org., Nano-Met. Chem.*, 2012, **42**, 251–255.

26 R. Nedjar, M. Borel and B. Raveau, *Z. Anorg. Allg. Chem.*, 1986, **541**, 198–204.

27 R. Nedjar, M. Borel and B. Raveau, *J. Solid State Chem.*, 1987, **71**, 451–457.

28 M. A. Bizeto, D. L. A. De Faria and V. R. L. Constantino, *J. Mater. Sci. Lett.*, 1999, **18**, 643–646.

29 X. Zhang, L. Liu, J. Ma, X. Yang, X. Xu and Z. Tong, *Mater. Lett.*, 2013, **95**, 21–24.

30 H. Pan, X. Li, Z. Zhuang and C. Zhang, *J. Mol. Catal. A: Chem.*, 2011, **345**, 90–95.

31 X. Li, H. Pan, Q. Hu and C. Zhang, *J. Alloys Compd.*, 2011, **509**, 6252–6256.

32 X. Liu, W. Que, Y. Xing, X. Yin, Y. He and H. M. A. Javed, *J. Cryst. Growth*, 2015, **419**, 149–152.

33 H. Nakayama, M. Nose, S. Nakanishi and H. Iba, *J. Power Sources*, 2015, **287**, 158–163.

34 K. Nassau, J. Shiever and J. L. Bernstein, *J. Electrochem. Soc.*, 1969, **116**, 348–353.

35 F. Madaro, R. Saeterli, J. R. Tolchard, M.-A. Einarsrud, R. Holmestad and T. Grande, *CrystEngComm*, 2011, **13**, 1304–1313.

36 S. Suzuki, K. Teshima, A. Yamaguchi, K. Yubuta, T. Shishido and S. Oishi, *CrystEngComm*, 2012, **14**, 987–992.

37 G. Zhang, F. He, X. Zou, J. Gong, H. Tu, H. Zhang, Q. Zhang and Y. Liu, *J. Alloys Compd.*, 2007, **427**, 82–86.

38 T. M. Duarte, L. M. C. Honorio, A. S. Brito, J. K. D. Souza, E. Longo, R. L. Tranquilin, A. G. Souza, I. M. G. Santos and A. S. Maia, in *Brazil Mrs Meeting 2014*, 2015, vol. 97, p. 012001.

39 C. M. Papa, A. J. Cesnik, T. C. Evans and K.-S. Choi, *Langmuir*, 2015, **31**, 9502–9510.

40 J. F. Liu, X. L. Li and Y. D. Li, *J. Cryst. Growth*, 2003, **247**, 419–424.

41 Z. Y. Zhan, C. Y. Xu, L. Zhen, W. S. Wang and W. Z. Shao, *Ceram. Int.*, 2010, **36**, 679–682.

42 L. Li, J. Deng, J. Chen, X. Sun, R. Yu, G. Liu and X. Xing, *Chem. Mater.*, 2009, **21**, 1207–1213.

43 L. Li, J. Deng, R. Yu, J. Chen, X. Wang and X. Xing, *Inorg. Chem.*, 2010, **49**, 1397–1403.

44 B. Gao, J. Fu, K. Huo, W. Zhang, Y. Xie and P. K. Chu, *J. Am. Ceram. Soc.*, 2011, **94**, 2330–2338.

45 A. Rousseau, V. Laur, M. Guilloux-Viry, G. Tanné, F. Huret, S. Députier, A. Perrin, F. Lalu and P. Laurent, *Thin Solid Films*, 2006, **515**, 2353–2360.

46 C. Maréchal, E. Lacaze, W. Seiler and J. Perriére, *Phys. C*, 1998, **294**, 23–32.

47 E. Irle, R. Blachnik and B. Gather, *Thermochim. Acta*, 1991, **179**, 157–169.

48 M. Gasperin and M. Le Bihan, *J. Solid State Chem.*, 1982, **43**, 346–353.

49 G. Fallon, B. Gatehouse and L. Guddat, *J. Solid State Chem.*, 1986, **61**, 181–187.

50 N. Kumada and N. Kinomura, *Eur. J. Solid State Inorg. Chem.*, 1997, **34**, 65–72.

51 P. Appendino, M. Montorsi and M. Vallino, *Ann. Chim.*, 1976, **66**, 417–427.

52 A. Waroquet, PhD Thesis Dissertation, Université de Rennes 1, 2015.

53 R. Paria Sena, A. A. Babaryk, S. Khainakov, S. Garcia-Granda, N. S. Slobodyanik, G. Van Tendeloo, A. M. Abakumov and J. Hadermann, *Dalton Trans.*, 2016, **45**, 973–979.

54 H. Fujioka, in *Handbook of Crystal Growth*, North-Holland, Boston, 2nd edn, 2015, pp. 365–397.

55 C. Xu, S. Wicklein, A. Sambri, S. Amoruso, M. Moors and R. Dittmann, *J. Phys. D: Appl. Phys.*, 2014, **47**, 034009.

56 G. Wulff, *Z. Kristallogr. - Cryst. Mater.*, 2015, **34**, 449.

57 *Handbook of crystal growth*, G. Dhanaraj, K. Byrappa, V. Prasad and M. Dudley, Springer Berlin Heidelberg, Berlin, Heidelberg, 2010.

58 Q. Simon, V. Dorcet, P. Boullay, V. Demange, S. Députier, V. Bouquet and M. Guilloux-Viry, *Chem. Mater.*, 2013, **25**, 2793–2802.

59 M. Lundberg and M. Sundberg, *J. Solid State Chem.*, 1986, **63**, 216–230.

60 C.-Y. Xu, L. Zhen, L. Yang, K. He, W.-Z. Shao and L.-C. Qin, *Ceram. Int.*, 2008, **34**, 435–437.

61 C.-Y. Xu, L. Zhen, R. Yang and Z. L. Wang, *J. Am. Chem. Soc.*, 2007, **129**, 15444–15445.

62 J. Narayan, K. Dovidenko, A. K. Sharma and S. Oktyabrsky, *J. Appl. Phys.*, 1998, **84**, 2597–2601.

63 M. Nistor, N. B. Mandache, J. Perrière, C. Hebert, F. Gherendi and W. Seiler, *Thin Solid Films*, 2011, **519**, 3959–3964.

64 R. Abe, M. Hara, J. N. Kondo, K. Domen, K. Shinohara and A. Tanaka, *Chem. Mater.*, 1998, **10**, 1647–1651.

65 Y. Hosogi, H. Kato and A. Kudo, *J. Phys. Chem. C*, 2008, **112**, 17678–17682.

66 H. Takahashi, M. Kakihana, Y. Yamashita, K. Yoshida, S. Ikeda, M. Hara and K. Domen, *Phys. Chem. Chem. Phys.*, 2000, **2**, 4461–4464.

67 A. S. Gilbert and N. Sheppard, *J. Chem. Soc. D*, 1971, 337–338.

68 M. Hashimoto, G. Koyano and N. Mizuno, *J. Phys. Chem. B*, 2004, **108**, 12368–12374.